Energetics of nonequilibrium solidification in Al-Sm

S. H. Zhou[1] and R. E. Napolitano[1,2]
[1]*Materials Sciences, Ames Laboratory, USDOE, Ames, Iowa 50011, USA*
[2]*Department of Materials Science and Engineering, Iowa State University, Ames, Iowa 50011, USA*
(Received 28 July 2008; published 21 November 2008)

Solution-based thermodynamic modeling, aided by first-principles calculations, is employed here to examine phase transformations in the Al-Sm binary system which may give rise to product phases that are metastable or have a composition that deviates substantially from equilibrium. In addition to describing the pure undercooled Al liquid with a two-state model that accounts for structural ordering, thermodynamic descriptions of the fcc phase, and intermediate compounds (Al_4Sm-β, $Al_{11}Sm_3$-α, Al_3Sm-δ, and Al_2Sm-σ) are reanalyzed using special quasirandom structure and first-principles calculations. The possible phase compositions are presented over a range of temperatures using a "Baker-Cahn" analysis of the energetics of solidification and compared with reports of rapid solidification. The energetics associated with varying degrees of chemical partitioning are quantified and compared with experimental observations of the metastable $Al_{11}Sm_3$-α primary phase and reports of amorphous solids.

DOI: 10.1103/PhysRevB.78.184111 PACS number(s): 64.70.D−, 64.70.kd, 64.60.Q−, 64.30.Ef

I. INTRODUCTION

Both glassy phases and nonequilibrium crystalline phases have been observed to readily form in Al-Sm alloys upon rapid cooling from the melt[1–3] with corresponding single and multiphase nanoscale structures. An understanding of the phase competition and selection in this and other glass forming systems with many avenues for melt relaxation requires accurate descriptions of system thermodynamics and transformation kinetics. Previously, we have reported on (i) the detailed modeling of thermodynamic properties of the Al-Sm binary system along with the binary phase diagram showing both stable and metastable phase boundaries[4] and (ii) the stability of the intermetallic phases with $Al_{11}Sm_3$ or Al_4Sm stoichiometry with respect to the undercooled liquid.[5] In the current paper, we refine the reported models further and compute the associated properties of the system, specifically examining the limits of nonequilibrium partitioning during crystallization from the melt, the possible composition ranges for stable and metastable phases and the associated driving forces.

The Al-Sm binary system has received much attention with respect to its compositional range of glass forming ability (GFA), a poorly defined property that is a measure of the competitiveness of crystalline phase formation kinetics relative to the tendency for the liquid to become glassy at high undercoolings. To this point, several recent reports illustrate the importance of understanding nonequilibrium solidification of crystalline phases in this system. In one investigation,[5] the metastable $Al_{11}Sm_3$-α was observed as the primary phase during copper chill casting, rather than the stable Al_3Sm-δ phase, in an Al-18 at.% Sm alloy. Also, nonequilibrium compositions in the Al-fcc phase have been reported in melt-spun ribbons[6] where effective partition coefficient values of 0.0122 and 0.0346 were measured for copper-wheel free-jet melt-spinning rates of 10 and 40 m/s, respectively, showing considerable deviation from the equilibrium partition coefficient of ~0.001.[4] Transmission electron microscopy and atom-probe investigation of melt-spun ribbons Al-10 at.% Sm have also shown nanoscale crystalline clusters of various composition.[7] These experimental reports clearly suggest that conditions of local chemical equilibrium do not apply at the high undercoolings (cooling rates) that are important for quantifying the competition between crystalline and glassy phases. Indeed, such assessment requires that a hierarchy of scenarios, representing increasing departure from equilibrium, be considered. This necessarily includes evaluation of equilibrium crystalline phases, metastable crystalline phases with constrained equilibrium compositions, nonequilibrium composition of both stable and metastable crystalline phases, and noncrystalline phases, all with respect to the undercooled alloy liquid. In the following analysis, a quantitative comparison of the energetics associated with stable and metastable crystalline phases over the full range of equilibrium and nonequilibrium compositions is presented. In addition, using the developed thermodynamic framework, the implications with respect to transformation kinetics and glass formation are examined.

II. THERMODYNAMIC MODELING

In our previous work,[4] we developed a thermodynamic model for the Al-Sm system, in which the liquid phase was described using a three-species association model, the intermediate phases were treated as stoichiometric compounds, and the terminal phases were treated as solid solutions with a single sublattice model. In addition to the stable phases, thermodynamic descriptions of the metastable $Al_{11}Sm_3$-α and Al_4Sm-γ phases were developed, and both stable and metastable phase equilibria were presented over the full composition range, providing a general model which is consistent with available experimental data. Here, with the principal aim being to quantify the relative energetics of stable and metastable phases that may form from a highly undercooled melt, we focus specifically on the undercooled liquid and the crystalline phases that may form upon quenching. Improving on the previous model, a two-state description is incorporated into the association model described in Ref. 4 for the liquid phase, and a two-sublattice model is employed to de-

TABLE I. Summary of the thermodynamic models used for the Al-Sm binary system.

Phase	Prototype	Method (Formulation)	Model
Liquid		Association model (Al, Al_2Sm, Sm)	${}^{ref}G_m^L = \sum_i x_i {}^0G_i^L$, ($x_i$ is overall composition); ${}^{id}G_m^L = \frac{RT}{1+2y_{Al_2Sm}} \sum_i y_i \ln y_i$; ${}^{xs}G_m^L = \frac{1}{1+2y_{Al_2Sm}} (\sum_i \sum_{j>i} y_i y_j {}^0L_{i,j}^L + y_{Al_2Sm} \Delta G^0_{Al_2Sm})$ ($i,j = Al, Al_2Sm, Sm$); (y_i is mole fraction of species i)
Al-fcc	Cu	One-sublattice model $(Al, Sm)_1$	${}^{ref}G_m^\phi = \sum_{i=Al,Sm} x_i {}^\circ G_i^\phi$; ${}^{id}G_m^\phi = RT \sum_{i=Al,Sm} x_i \ln x_i$; ${}^{xs}G_m^\phi = x_{Al}x_{Sm} \sum_{j=0}^{n} {}^jL_{Al,Sm}^\phi (x_{Al} - x_{Sm})^j$
Sm-rho	α-Sm		
Sm-bcc	W		
		Two-sublattice model	
$Al_{11}Sm_3$-α	$Al_{11}La_3$-α	$(Al, Sm)_{0.786}(Al, Sm)_{0.214}$	${}^{ref}G_m^\phi = \sum_{i=Al,Sm} y_i^I \sum_{j=Al,Sm} y_j^{II} {}^\circ G_{i:j}^\phi$; ${}^{id}G_m^\phi = RT \sum_{i=Al,Sm} (m y_i^I \ln y_i^I + n y_i^{II} \ln y_i^{II})$; ${}^{xs}G_m^\phi = y_{Al}^I y_E^I \sum_{i=Al,Sm} y_i^{II} \sum_{k=0} {}^kL_{Al,Sm:i}^\phi (y_{Al}^I - y_{Sm}^I)^k + y_{Al}^{II} y_{Sm}^{II} \sum_{i=Al,Sm} y_i^I \sum_{k=0} {}^kL_{i:Al,Sm}^\phi (y_{Al}^{II} - y_{Sm}^{II})^k$
Al_4Sm-β	Al_4Ba	$(Al, Sm)_{0.8}(Al, Sm)_{0.2}$	
Al_3Sm-δ	Ni_3Sn	$(Al, Sm)_{0.75}(Al, Sm)_{0.25}$	
Al_2Sm-σ	Cu_2Mg	$(Al, Sm)_{0.67}(Al, Sm)_{0.33}$	
		Stoichiometric phases	
AlSm-θ	AlEr	$(Al)_{0.5}(Sm)_{0.5}$	$G_m^\phi = \Delta G^\phi_{Al_pSm_q} + p^\circ G_{Al}^{fcc} + q^\circ G_{Sm}^{rho} = a^\phi + b^\phi T + p^\circ G_{Al}^{fcc} + q^\circ G_{Sm}^{rho}$
$AlSm_2$-χ	Co_2Si	$(Al)_{0.33}(Sm)_{0.67}$	
Al_4Sm-γ	Al_4U	$(Al)_{0.8}(Sm)_{0.2}$	

scribe the thermodynamic behavior of the $Al_{11}Sm_3$-α, Al_4Sm-β, Al_3Sm-δ, and Al_2Sm-σ phases over the full composition range. The model parameters, describing the Gibbs free energies of the unstable end members of the compounds, are determined using first-principles calculations. To determine the Gibbs free energy of the fcc solution phase more accurately, the interaction parameter is evaluated with its enthalpy of mixing, which is computed from the first-principles calculation for the fcc special quasirandom structure (SQS) reported by Zunger *et al.*,[8,9] The resulting equilibrium phase diagram is presented and followed by a detailed analysis of the model implications with respect to metastable phases and nonequilibrium chemical partitioning. A Baker-Cahn framework[10,11] is employed to represent the relevant composition domains, and the transformation driving forces for both single-phase and two-phase solidification are computed as a function of composition. Results are compared with previously reported experimental observation of chemical partitioning, phase selection, and glass formation.

A. Model formulation

The present thermodynamic formulation is built on our previously reported model for the Al-Sm system.[4] The distinguishing features of the current model are (i) a two-sublattice model[12] for the Al_4Sm-β, $Al_{11}Sm_3$-α, Al_3Sm-δ, and Al_2Sm-σ compounds and (ii) a two-state treatment[13–15] for the undercooled pure Al liquid. The thermodynamic models are defined in Table I where the total Gibbs free energy for any phase, ϕ, is generally given by the sum of three contributions,

$$G_m^\phi = {}^{ref}G_m^\phi + {}^{id}G_m^\phi + {}^{xs}G_m^\phi, \quad (1)$$

where the subscript, m, indicates that all terms are molar quantities. The first term in Eq. (1) is the sum of occupancy-

weighted sublattice end-member contributions, while the second and third terms are the ideal and excess parts of the Gibbs free energy of mixing, respectively. Thermodynamic functions for the pure element states are taken from the Refs. 4, 13, and 16, as listed in Table II. The specific treatment of each phase is discussed briefly here.

Previously reported models for the Al liquid phase[13] exhibit a discontinuity in the slope of the heat capacity vs temperature curve at T_m. To address this problem, a two-state approach[13–15] is taken here, where the undercooled liquid Al (L') is treated as an ideal mixture of "solidlike" and "liquidlike" particles. The parameters in Ref. 13 are used here, as listed in Table II. For the Gibbs free energy of mixing in the liquid solution phase, we employ a three-species (Al, Al_2Sm, and Sm) association model from Ref. 4 as described in Table I.

The fcc, bcc, and rho terminal solid solution phases are treated as simple binary substitutional solutions with the model described in Table I and the model parameters listed in Table III. We employ the thermodynamic descriptions for the rho and bcc phases from Ref. 4 and compute the $j=0$ term for the fcc phase by treating ${}^0L^{\mathrm{fcc}}_{\mathrm{Al,Sm}}$ as a constant (i.e., a regular solution). The intermetallic phases, $Al_4Sm(\beta)$, $Al_{11}Sm_3(\alpha)$, $Al_3Sm(\delta)$, and $Al_2Sm(\sigma)$, are described as two-sublattice solid solutions with the form $(\mathrm{Al,Sm})_m(\mathrm{Al,Sm})_n$. The associated Gibbs free energies are modeled as shown in Table I. Given this formulation, sublattice end members include four different stoichiometries (Al_mAl_n, Al_mSm_n, Sm_mAl_n, and Sm_mSm_n) with only one being the stable compound for each phase [i.e., $Al_4Sm(\beta)$, $Al_{11}Sm_3(\alpha)$, $Al_3Sm(\delta)$, and $Al_2Sm(\sigma)$].

The intermediate phases AlSm-θ, $AlSm_2$-χ, and Al_4Sm-γ are treated as stoichiometric compounds with their Gibbs free energies given in Table I, where $\Delta G^{\phi}_{\mathrm{Al}_p\mathrm{Sm}_q}$ is the Gibbs free energy of formation for the compound Al_pSm_q, modeled as a linear function of temperature.

B. Model parameters

As described in the preceding section, the model formulation for the phases in Table I includes a total of nine temperature-dependent standard free energy (${}^{\circ}G^{\phi}$) parameters (Table II), seven interaction parameters (${}^{i}L^{\phi}$), and twenty Gibbs free energy of formation parameters (ΔG^{ϕ}), as listed in Table III. The standard Gibbs free-energy parameters of pure Al and Sm in the relevant phases in Table II were obtained from the indicated sources. In this section, we describe our methods for evaluation of the remaining 27 model parameters listed in Table III.

The coefficients for the stable end members (${}^{\circ}G^{\beta}_{\mathrm{Al:Sm}}$, ${}^{\circ}G^{\alpha}_{\mathrm{Al:Sm}}$, ${}^{\circ}G^{\delta}_{\mathrm{Al:Sm}}$, and ${}^{\circ}G^{\sigma}_{\mathrm{Al:Sm}}$) reported in Ref. 4 are used here. These were evaluated from available enthalpy of formation[17,18] and phase equilibrium data.[19,20] With no available data for the remaining unstable end members (Al_mAl_n, Sm_mAl_n, and Sm_mSm_n), we treat them as constants and quantify them using first-principles calculations of zero-Kelvin enthalpies of formation. To calculate the zero-Kelvin enthalpies of formation, the total energy of the associated phases, along with the Al-fcc and Sm-rho references, are computed using the Vienna *ab initio* simulation package (VASP) (Ref. 21) code with the high-precision generalized gradient approximation (GGA).[22] Brillouin-zone integrations are performed using Monkhorst-Pack k-point $12\times12\times12$ meshes for the Al-fcc, Sm-rho, Al_3Sm-δ, and Al_4Sm-β, $6\times6\times6$ meshes for $Al_{11}Sm_3$-α, and $15\times15\times15$ meshes for Al_2Sm-σ. Relaxation is performed only with respect to specific volume due to their instability. Consequently, the enthalpy of formation (ΔH^{ϕ}_f) for a given compound is calculated as the difference between the energy (E^{ϕ}) of the compound ϕ and linear combination of the pure element reference state energies $E^{\mathrm{fcc}}_{\mathrm{Al}}$ and $E^{\mathrm{rho}}_{\mathrm{Sm}}$,

$$\Delta H^{\phi}_f = E^{\phi} - x_{\mathrm{Al}}E^{\mathrm{fcc}}_{\mathrm{Al}} - x_{\mathrm{Sm}}E^{\mathrm{rho}}_{\mathrm{Sm}}. \quad (2)$$

The results are summarized in Table IV and used to determine the parameters of the unstable end members listed in Table III. By assuming a small homogeneous composition range for the stable σ phase, the positive interaction parameter ${}^0L^{\sigma}_{\mathrm{Al,Sm:Sm}}$ is evaluated.

The Gibbs free energy of the fcc solution phase is important for us to determine the fcc formation driving force and further to predict the possible amorphous composition range and maximum extent of Sm trapping in Al-fcc (see Sec. IV). However, there are no experimental data available for the excess Gibbs free energy of this phase. The enthalpies of mixing for the Al-fcc phase, therefore, are calculated from first principles using three 16-atom fcc SQSs (Refs. 8 and 9) for a composition of $x_{\mathrm{Sm}}=0.25$. The concept of SQS was proposed by Zunger *et al.*[8] to mimic a random solution phase by reproducing the pair and multiple-body correlations using a small size supercell. The fcc SQS solution structures generated by Wei *et al.*[9] are employed in this work. The energetics of the fcc SQS are computed using the GGA pseudopotentials with VASP.[21] Using the same argument as that for the unstable end members of the compounds, we only relax the cell volume of the fcc SQS. The calculated enthalpy of mixing for the Al-fcc phase at composition $Al_{0.75}Sm_{0.25}$ listed in Table IV is used to evaluate the parameter ${}^0L^{\mathrm{fcc}}_{\mathrm{Al,Sm}}$ in Table III, considering dilute effects only.

III. RESULTS AND ANALYSIS

The equilibrium binary phase diagram is plotted in Fig. 1, showing that the model refinement does not significantly alter the equilibrium phase boundaries. Using this model, we begin an examination of nonequilibrium partitioning with respect to the formation of all crystalline phases from the liquid. As an example, the free energies for the liquid and σ phases at $T=806$ K are shown in Fig. 2. The two equilibrium liquidus compositions (x^L_{Eq}) are shown on this figure, bounding the full range of homogeneous liquid compositions for which there is a positive driving force for the formation of the σ phase. This range includes two important regimes where (i) some degree of chemical partitioning is required (P range) and (ii) partitionless solidification may be observed (PL range). Each partitioning range is bounded by a liquidus composition (x^L_{Eq}) and the corresponding x_0 composition, representing the two relevant extremes with respect to requirements for diffusion. The x^L_{Eq} composition represents the

TABLE II. Coefficients for the standard Gibbs free energies of pure Al and Sm in the relevant phases. Each Gibbs free energy is described as ${}^0G_i^{\phi}={}^0G_i^{\mathrm{ref}}+a_0+a_1T+a_2T\ln T+a_3T^2+a_4T^3+a_5T^4+a_6T^{-1}+a_7T^{-9}-a_8RT\ln(1+e^{-\varepsilon/RT})$ (J/mol).

	${}^0G_{\mathrm{Al}}^{L'}$ [a]	${}^0G_{\mathrm{Al}}^{L}$ [b]		${}^0G_{\mathrm{Al}}^{\mathrm{fcc}}$ [b]		${}^0G_{\mathrm{Al}}^{\mathrm{bcc}}$ [b]
$T_{\min}$	298	933.47	298	700	933.47	298
$T_{\max}$	933.47	3200	700	933.47	2900	3200
${}^0G_i^{\mathrm{ref}}$	${}^0G_{\mathrm{Al}}^{\mathrm{fcc}}$					${}^0G_{\mathrm{Al}}^{\mathrm{fcc}}$
a_0	5740.24277	−795.996	7976.15	−11276.24	−11278.37	10083
a_1	56.8484223	177.430178	137.093038	223.048446	188.68415	−4.813
a_2	−10.1893882	−31.748192	−24.3671976	−38.5844296	−31.74819	
a_3	0.10055155		−0.001884662	0.018531982		
a_4			-8.77664×10^{-7}	-5.76422×10^{-6}		
a_5						
a_6			74092	74092		
a_7					-1.2305×10^{28}	
a_8	1					
ε	5176.85-RT					
	${}^0G_{\mathrm{Al}}^{\mathrm{rho}}$ [c]	${}^0G_{\mathrm{Sm}}^{L}$ [b]			${}^0G_{\mathrm{Sm}}^{\mathrm{bcc}}$ [b]	
$T_{\min}$	298	298	1190	298	1190	1345
$T_{\max}$	3200	1190	2100	1190	1345	2100
${}^0G_i^{\mathrm{ref}}$	${}^0G_{\mathrm{Al}}^{\mathrm{fcc}}$					
a_0	2283.5	3468.783	−11728.229	−4368.72	−15957.862	111191.653
a_1		20.117456	273.48707	55.972523	253.121044	−624.680805
a_2		−11.696828	−50.208	−16.929849	−46.9445	71.6856914
a_3		−0.032418177		−0.02544601		−0.004731496
a_4		4.54427×10^{-6}		3.5795×10^{-6}		3.32986×10^{-6}
a_5						
a_6		23528		94209		−24870276
a_7						
a_8						
ε						
			${}^0G_{\mathrm{Sm}}^{\mathrm{rho}}$ [b]		${}^0G_{\mathrm{Sm}}^{\mathrm{fcc}}$ [c]	
$T_{\min}$	298	700	1190	1345	298	
$T_{\max}$	700	1190	1345	2100	2100	
${}^0G_i^{\mathrm{ref}}$					${}^0G_{\mathrm{Sm}}^{\mathrm{rho}}$	
a_0	−3872.013	−50078.215	289719.819	−23056.079	890	
a_1	−32.10748	627.869894	−2744.50976	282.194375		
a_2	−1.6485	−102.665	381.41982	−50.208		
a_3	−0.050254	0.0474522	−0.254986338			
a_4	1.01035×10^{-5}	-7.5384×10^{-6}	2.751215×10^{-5}			
a_5						
a_6	−82168	3861770	−40102102			
a_7						
a_8						
ε						

[a]Reference 13.
[b]Reference 16.
[c]Reference 4.

TABLE III. Evaluated thermodynamic model parameters (in SI unit).

Phase	Parameter	Value (J/mol)	Ref.
Liquid	${}^0L^{\mathrm{liq}}_{\mathrm{Al,Sm}}$	−80524	4
	${}^0L^{\mathrm{liq}}_{\mathrm{Al,Al_2Sm_1}}$	−26012	4
	${}^0L^{\mathrm{liq}}_{\mathrm{Al_2Sm_1,Sm}}$	−42022	4
	$\Delta G^0_{\mathrm{Al_2Sm_1}}$	−144212+35.854 T	4
bcc	${}^0L^{\mathrm{bcc}}_{\mathrm{Al,Sm}}$	−57431	4
	${}^1L^{\mathrm{bcc}}_{\mathrm{Al,Sm}}$	*18102*	4
fcc	${}^0L^{\mathrm{fcc}}_{\mathrm{Al,Sm}}$	−7463	
Al_4Sm-β	$\Delta G^{\beta}_{\mathrm{Al:Al}}$	18610	This work
	$\Delta G^{\beta}_{\mathrm{Al:Sm}}$	−23121−6.202 T	4
	$\Delta G^{\beta}_{\mathrm{Sm:Al}}$	29451.8	4
	$\Delta G^{\beta}_{\mathrm{Sm:Sm}}$	25555.6	4
$Al_{11}Sm_3$-α	$\Delta G^{\alpha}_{\mathrm{Al:Al}}$	21708	This work
	$\Delta G^{\alpha}_{\mathrm{Al:Sm}}$	−34800+1.344 T	4
	$\Delta G^{\alpha}_{\mathrm{Sm:Al}}$	31451.8	4
	$\Delta G^{\alpha}_{\mathrm{Sm:Sm}}$	27555.6	4
Al_3Sm-δ	$\Delta G^{\delta}_{\mathrm{Al:Al}}$	17840	This work
	$\Delta G^{\delta}_{\mathrm{Al:Sm}}$	−48386+8.342 T	4
	$\Delta G^{\delta}_{\mathrm{Sm:Al}}$	−18922.5	4
	$\Delta G^{\delta}_{\mathrm{Sm:Sm}}$	4855	4
Al_2Sm-σ	$\Delta G^{\sigma}_{\mathrm{Al:Al}}$	14650	This work
	$\Delta G^{\sigma}_{\mathrm{Al:Sm}}$	−55000+7.382 T	4
	$\Delta G^{\sigma}_{\mathrm{Sm:Al}}$	14202	4
	$\Delta G^{\sigma}_{\mathrm{Sm:Sm}}$	8801	4
	${}^0L^{\sigma}_{\mathrm{Al,Sm:Sm}}$	22000	This work
Al_4Sm-γ	$\Delta G^{\gamma}_{\mathrm{Al:Sm}}$	−28535	4
AlSm-ϑ	$\Delta G^{\theta}_{\mathrm{Al:Sm}}$	−49000+9.446 T	4
$AlSm_2$-χ	$\Delta G^{\chi}_{\mathrm{Al:Sm}}$	−37300+8.799 T	4

full chemical equilibrium or "infinite diffusion time" limit, where ${}^{\mathrm{eq}}\mu^{\mathrm{liq}}_{\mathrm{Sm}} = {}^{\mathrm{eq}}\mu^{\phi}_{\mathrm{Sm}}$. The x_0^1 and x_0^2 compositions are defined by the criterion $G^{\mathrm{liq}}_m = G^{\mathrm{sol}}_m$ bounding the PL range, over which ${}^0G^{\mathrm{liq}}_m > {}^0G^{\phi}_m$ such that the liquid phase *may* transform directly into the solid phase in a diffusionless manner. Thus, this range represents the "zero diffusion time" limit. Over a range of temperatures, these limiting compositions define the equilibrium liquidus (T_L) curves and the so-called T_0 curves. These are plotted in Fig. 3, in comparison with reported data from experimental observation of glass formation[3] and devitrification,[1,23,24] where it is evident, as previously suggested[13] that the T_0 curves provide a practical limit for partitionless crystallization.

Focusing now on the P range from the standpoint of required diffusion time, we recognize that the limits in Fig. 3 represent only the two-terminal cases and that a continuum should exist between them, as determined by the *degree* of chemical partitioning. To describe this continuum, we introduce a parameter, η, defined as

TABLE IV. A summary of results from first-principles calculations.

Phase	Prototype	Formula	First-principles ΔH (kJ/mol)
Al-fcc	Cu	Al	0
Sm-rho	Sm	Sm	0
Al_2Sm-σ		Al_2Al	14.7
		Sm_2Al	14.2
	Cu_2Mg	Sm_2Sm	8.8
Al_3Sm-δ		Al_3Al	17.8
		Sm_3Al	−18.9
	Ni_3Sn	Sm_3Sm	4.9
Al_4Sm-β		Al_4Al	18.6
		Sm_4Al	29.5
	Al_4Ba	Sm_4Sm	25.6
$Al_{11}Sm_3$-α		$Al_{11}Al_3$	21.7
		$Sm_{11}Al_3$	31.5
	$Al_{11}La_3$-α	$Sm_{11}Sm_3$	27.6
$Al_{0.75}Sm_{0.25}$	SQS 16-fcc	$Al_{0.75}Sm_{0.25}$	−1.2

$$\eta = \frac{\mu^{\mathrm{liq}}_{\mathrm{Sm}} - {}^0\mu^{\mathrm{liq}}_{\mathrm{Sm}}}{{}^{\mathrm{eq}}\mu^{\mathrm{liq}}_{\mathrm{Sm}} - {}^0\mu^{\mathrm{liq}}_{\mathrm{Sm}}}, \tag{3}$$

which is inversely related to chemical supersaturation in the liquid phase, as shown in Fig. 2, for a liquid of composition

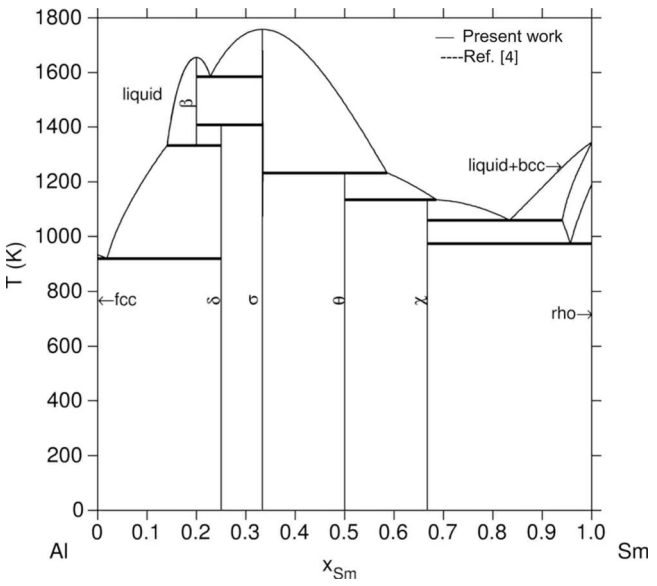

FIG. 1. The Al-Sm binary phase diagram, computed using the present model. While the current model is better able to describe nonequilibrium phase compositions, the equilibrium phase boundaries are indistinguishable from those which result from our previously reported model (Ref. 4).

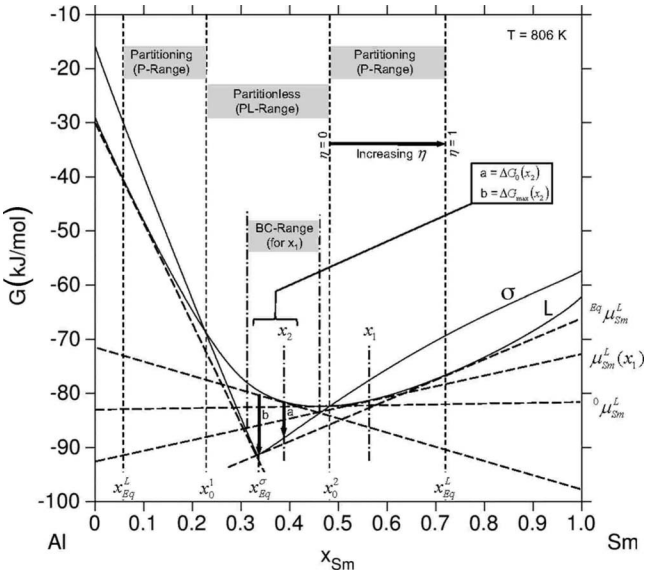

FIG. 2. The Gibbs free energies of the liquid (l) and $Al_2Sm(\sigma)$ phases at (806 K) computed with the present model.

$x_{Sm}^{liq}=x_1$. For a given temperature, the variation in η from 0 to 1 indicates the increasing *minimum* diffusional burden that accompanies the solidification transition as we consider liquid compositions across the partitioning range, from T_0 to T_L. Thus, level curves with respect to η in the composition-temperature domain represent effective liquidus or "crystallization composition" curves associated with a particular degree of constraint on the level of supersaturation that can be relieved by diffusion. In Fig. 4(a), we plot the full crystallization surface comprised of these level curves, varying from the liquidus curve at $\eta=1$ to the T_0 curve at $\eta=0$. An isothermal section of this surface is shown in Fig. 4(b) for the σ phase at 600 K. We note further that the parameter, η, can be viewed, alternatively, as a time scale associated with the required diffusional relaxation, where $\eta=1$ corresponds to the infinite-time limit and $\eta=0$ corresponds to the zero-time limit. Thus, the effective crystallization surface which applies to any real process (i.e., one with a finite cooling rate) would be indicated by the appropriate constant-η section of the surface in Fig. 4(a). Examining this figure further reveals two important features. First, as the time scale decreases (i.e., the cooling rate increases), the primary phases that are likely to be observed shift in their applicable composition ranges. For example, the figure shows that the metastable $Al_{11}Sm_3$-α phase may be observed as the primary phase at low η, as we have previously reported.[5] Second, the composition range for which glass formation is likely becomes larger with decreasing η, as indicated in the figure by the region labeled "am," where glass formation has indeed been observed in this system.[1,23,24]

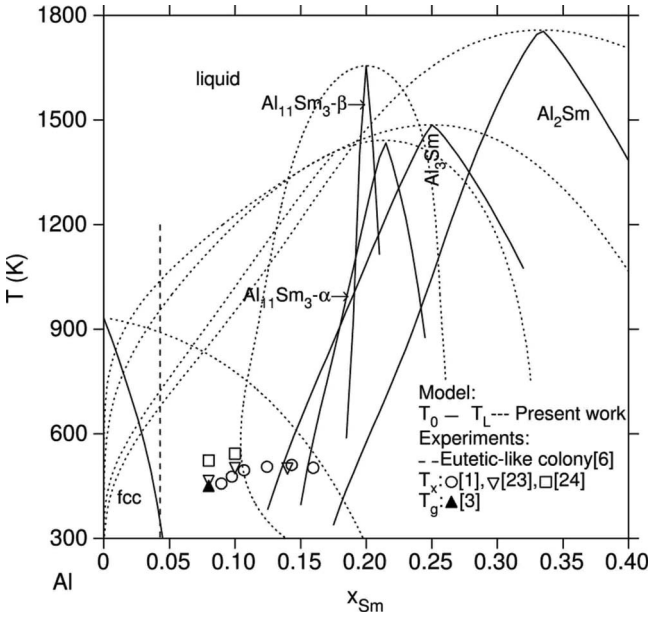

FIG. 3. The T_L and T_0 curves computed using present model.

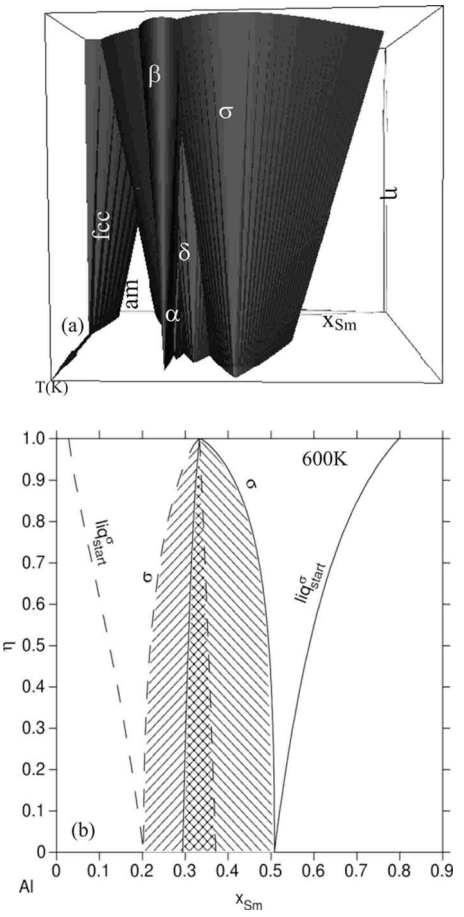

FIG. 4. (a) The crystallization surface showing the influence of initial supersaturation (indicated by η) on the effective liquidus. (b) An isothermal (600 K) section of (a) showing the effective liquidus curves varying from T_0 to T_L with increasing η and the associated range of possible σ crystallization compositions, as computed using the present model.

As we move away from the equilibrium liquidus and consider decreasing values of η, the increased chemical supersaturation permits an expanding range of solid compositions which may form directly from the liquid phase. These are indicated by the shaded regions in Fig. 4(b) for the σ phase at 600 K. Note here that the indicated range pertains only to

the "effective liquidus" which is the first liquid composition to reach a given value of η for a selected temperature. This explains why the outer curves in Fig. 4(b), for the σ phase, do not include the compositions (x_{Sm}) that lie between the two T_0 points (i.e., the PL range from x_0^1 to x_0^2) in Fig. 2. Alternatively, the Baker-Cahn construction[10,11] provides a clear framework for considering the range of permissible solid compositions which can initially crystallize from a given liquid composition, as indicated for $x_{Sm}^{liq}=x_1$, by the shaded band labeled "BC range" in Fig. 2. Thus, the possible associated composition pairs (x_{Sm}^{Liq} and x_{Sm}^{Sol}) are shown in Fig. 5(a) for several phases at 600 K. Here, we see that the allowable composition ranges for $Al_{11}Sm_3$-α, Al_4Sm-β, and Al_3Sm-δ overlap considerably, indicating phase competition at this temperature. For example, from a liquid of composition (x_{Sm}) between 0.104 and 0.262, any of these three phases may nucleate, with compositions lying within the respective ranges indicated. Similarly, the competition between $Al_{11}Sm_3$-α and Al_3Sm-δ extends over very large range, from $x_{Sm}=0.003$ up to $x_{Sm}=0.327$. In Fig. 5(b), we plot the composition ranges as a function of temperature showing how these overlapping regions may change with undercooling. Finally, in Fig. 5(c), the Baker-Cahn plots for three selected temperatures are compared with previously reported experimental data[6] where rapid solidification by free-jet melt-spinning yielded observed chemical partition coefficients of approximately 0.01–0.03 for the fcc phase in Al-Sm, much higher than the equilibrium partition coefficient.

It is important to note that Fig. 5 indicates only the phase composition pairs which give a net decrease in the Gibbs free energy and does not show the magnitude of the relevant driving force associated with any particular composition pair. As a prerequisite to computing any transformation kinetics, however, we must first compute these driving forces. Thus, the Baker-Cahn construction provides the bounds for the composition domain over which we must quantify the energetics. For example, the driving force (ΔG) for solidification, for the α, β, δ, σ, and fcc phases, is plotted in Fig. 6(a) over all possible liquid/solid composition pairs. This figure shows, for a given liquid, the dramatic change in the solidification driving force with solid composition. Clearly, the variation in driving force must be considered in concert with the changing diffusional burden as the transformation kinetics are compared across compositional domains. For example, a section of Fig. 6(a), taken on the plane defined by $x_{Sm}^{liq}=x_{Sm}^{sol}$, is shown in Fig. 6(b), comparing the free energies along a zero partitioning path where the diffusional burden vanishes completely. Under this constraint, we see that the α phase emerges from beneath the δ phase as temperature is increased from 600 to 1000 K.

Finally, we consider the driving force for the initial nucleation of the crystalline phase as a function of temperature for all possible solid compositions. The situation is shown in Fig. 7(a) for $x_{Sm}^{liq}=0.2$, where the upper and lower curves bounding the shaded region represent the zero partitioning case (ΔG_0), and the case where nucleation occurs at the composition associated with the maximum driving force (ΔG_{max}), respectively. These two quantities are illustrated graphically in Fig. 2 for an arbitrary composition, x_2. The net driving force for solidification with equilibrium partitioning

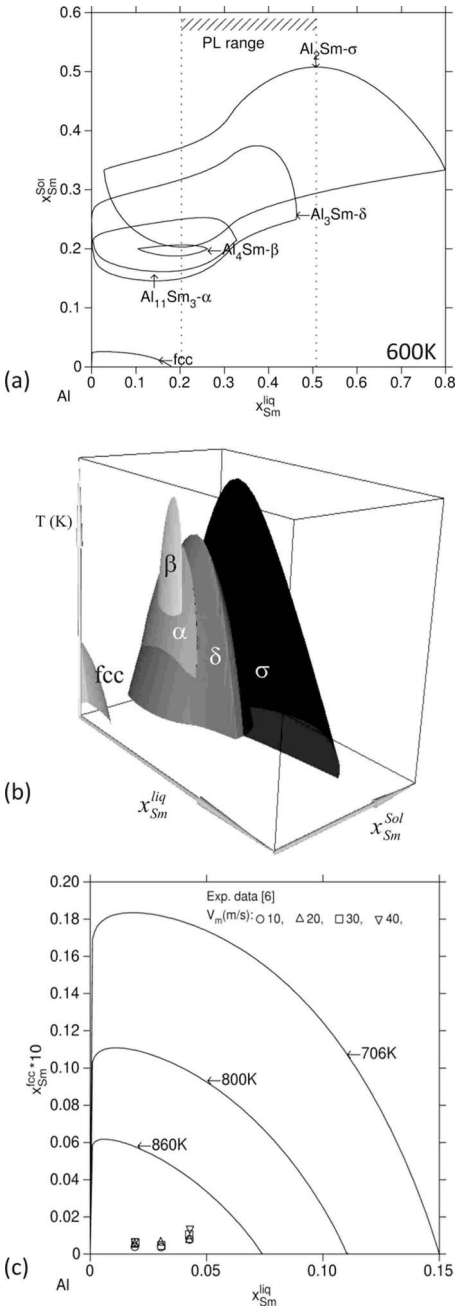

FIG. 5. The Baker-Cahn diagram showing permissible compositions for several crystalline phases (a) at 600 K, (b) over a range of temperatures, and (c) comparing measured fcc compositions in melt-spun ribbons to the permissible ranges computed for the estimated solidification temperatures (Ref. 6).

(ΔG_{eq}) is also shown in Fig. 7(a). Thus, the respective intercepts with the $\Delta G=0$ axis give the values of T_0 and T_L, as shown, and the shaded region between the curves represents the range of free energy available to drive the initial nucleation process, depending on the partitioning requirements which vary as the liquid composition passes from the P range into the PL range with decreasing temperature. The thick dashed curve in this figure is a schematic example of how the free energy actually "spent" to drive the nucleation process might change with temperature, as the degree of chemical

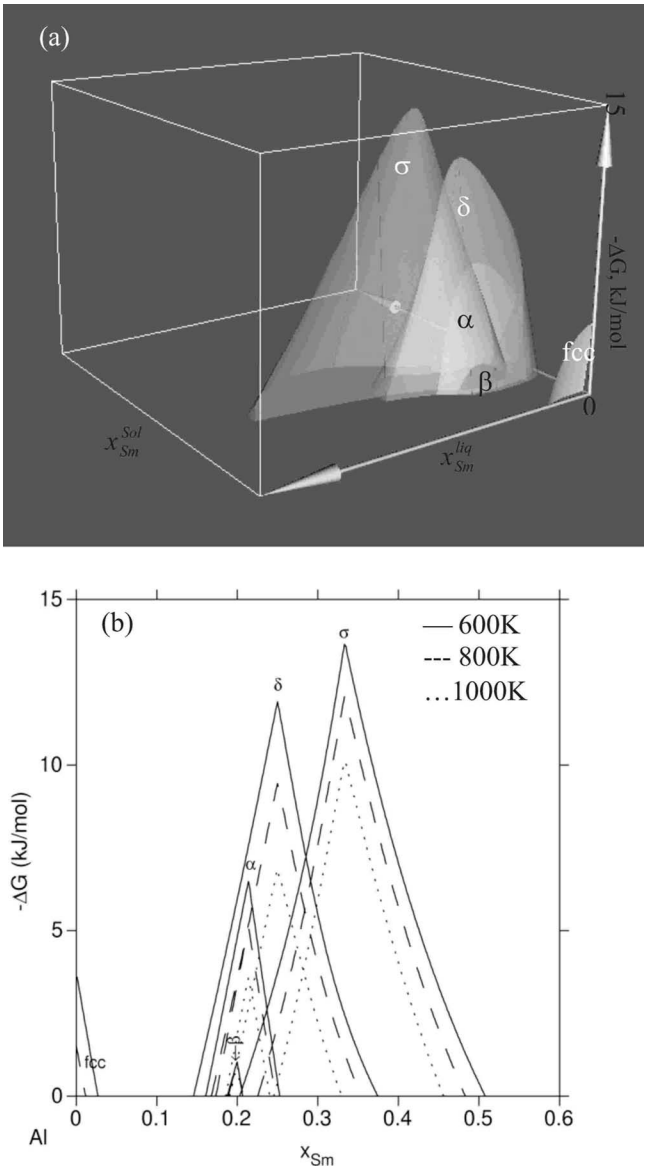

FIG. 6. The computed driving force for solidification of several crystalline phases at 600 K (a) over the full range of permissible compositions and (b) for the condition $x_{\mathrm{Sm}}^{\mathrm{liq}}=x_{\mathrm{Sm}}^{\mathrm{Sol}}$ at $T=600$, 800, and 1000 K.

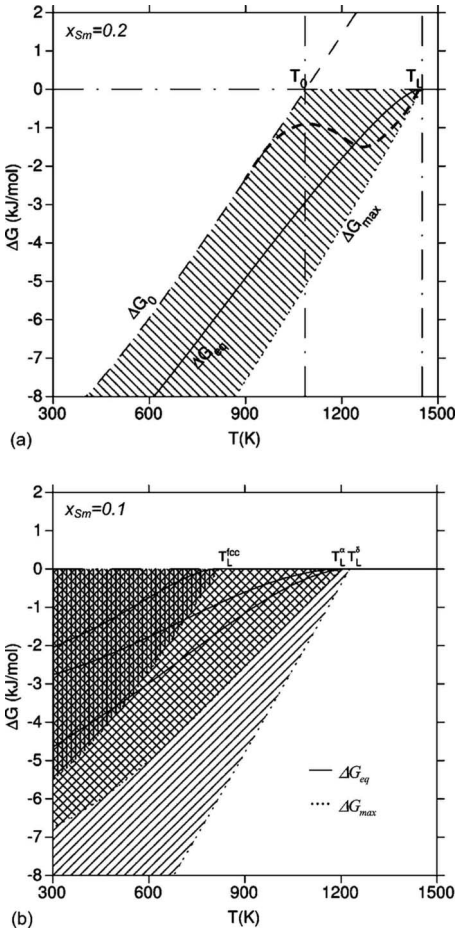

FIG. 7. (a) The computed driving force for δ solidification with a schematic (example) representation of how composition selection might occur (dashed curve), shown in terms of the fraction of available driving force spent on the process. (b) The computed driving force for solidification of the α, δ, and fcc phases from a liquid of composition $x_{\mathrm{Sm}}=0.1$.

partitioning varies. Understanding this allocation of the available driving force is a key issue in predicting and controlling phase competition/selection during rapid solidification and devitrification processes. The situation for $x_{\mathrm{Sm}}=0.10$ is plotted in Fig. 7(b) for three different solid phases (α, β, and δ). For each phase, the range of possible driving force is plotted as a function of temperature showing considerable overlap, indicating that prediction of phase selection must account for the kinetics associated with transformation over the broad range of driving forces concomitant with the variation in the degree of partitioning for each competing phase and that it is not appropriate to make arbitrary assumptions about composition selection (i.e., maximum driving force). We note the importance of the T_0 temperature as a bound for the entire selection region. Again, the decrease in the T_0 limit, as the composition is decreased from 0.20 to 0.10 shows that only highly partitioning options are available at the lower Sm concentrations, increasing the likelihood that an amorphous solid will be formed on rapid cooling, consistent with experimental observations.[1,23,24] Experimental measurement of the selected partitioning path for each phase, as suggested by the thick dashed curve in Fig. 7(a), remains as a critical step toward understanding the selection behavior in this and other systems.

IV. CONCLUSIONS

In the work reported here, thermodynamic models are refined and utilized to examine the energetics of the various competing processes associated with crystallization from the melt in the Al-Sm binary system. Specifically, the limits of nonequilibrium partitioning for stable and metastable phases and the associated driving forces are quantitatively assessed and compared. It is concluded that the full range of possible compositions for stable and metastable phases must be considered carefully in the prediction of phase selection and microstructural evolution during solidification from the melt (or

devitrification from the glassy state). Indeed, the competing effects of driving force and diffusional burden, along with their dependence on the composition of the crystallizing phase, calls into serious question any simple generalization (e.g., maximum driving force) of composition selection. Moreover, the quantitative assessment of composition-pair-dependent driving forces for the various relevant phases, as presented here, must be incorporated directly into kinetic models for meaningful prediction of phase and structure.

ACKNOWLEDGMENTS

This work was performed within the Ames Laboratory and was supported by the U.S. Department of Energy, Basic Energy Sciences, under Contract No. DE-AC02-07CH11358.

[1] A. Inoue, T. Zhang, K. Kita, and T. Masumoto, Mater. Trans., JIM **30**, 870 (1989).
[2] A. Inoue, Prog. Mater. Sci. **43**, 365 (1998).
[3] G. Wilde, H. Sieber, and J. H. Perepezko, J. Non-Cryst. Solids **250–252**, 621 (1999).
[4] S. H. Zhou and R. E. Napolitano, Metall. Mater. Trans. A **39**, 502 (2008).
[5] S. H. Zhou and R. E. Napolitano, Metall. Mater. Trans. A **38**, 1145 (2007).
[6] H. Meco and R. E. Napolitano, Mater. Sci. Forum **539-543**, 2810 (2007).
[7] Y. E. Kalay, L. S. Chumbley, and I. E. Anderson, J. Non-Cryst. Solids **354**, 3040 (2008).
[8] A. Zunger, S. H. Wei, L. G. Ferreira, and J. E. Bernard, Phys. Rev. Lett. **65**, 353 (1990).
[9] S. H. Wei, L. G. Ferreira, J. E. Bernard, and A. Zunger, Phys. Rev. B **42**, 9622 (1990).
[10] W. C. Carter and W. C. Johnson, in *The Thermodynamics of Solidification*, edited by J. C. Baker and J. W. Cahn (ASM Internaional, Materials Park, OH, 1971).
[11] J. C. Baker and J. W. Cahn, Acta Metall. **17**, 575 (1969).
[12] B. Sundman and J. Agren, J. Phys. Chem. Solids **42**, 297 (1981).
[13] S. H. Zhou and R. E. Napolitano, Acta Mater. **54**, 831 (2006).
[14] J. Agren, Phys. Chem. Liq. **18**, 123 (1988).
[15] J. Agren, B. Cheynet, M. T. Clavaguera-Mora, K. Hack, J. Hertz, F. Sommer, and U. R. Kattner, CALPHAD: Comput. Coupling Phase Diagrams Thermochem. **19**, 449 (1995).
[16] A. T. Dinsdale, CALPHAD: Comput. Coupling Phase Diagrams Thermochem. **15**, 317 (1991).
[17] C. Colinet, A. Pastural, and K. H. J. Buschow, J. Chem. Thermodyn. **17**, 1133 (1985).
[18] G. Borzone, A. M. Cardinale, A. Saccone, and R. Ferro, J. Alloys Compd. **220**, 122 (1995).
[19] A. Saccone, G. Cacciamani, D. Maccio, G. Borzone, and R. Ferro, Intermetallics **6**, 201 (1998).
[20] K. H. J. Buschow and J. H. N. van Vucht, Philips Res. Rep. **20**, 15 (1965).
[21] G. Kresse and D. Joubert, Phys. Rev. B **59**, 1758 (1999).
[22] J. P. Perdew, J. A. Chevary, S. H. Vosko, K. A. Jackson, M. R. Pederson, D. J. Singh, and C. Fiolhais, Phys. Rev. B **46**, 6671 (1992).
[23] J. Q. Guo, K. Ohtera, K. Kita, J. Nagahora, and N. S. Kazama, Mater. Lett. **24**, 133 (1995).
[24] P. Rizzi, M. Baricco, S. Borace, and L. Battezzati, Mater. Sci. Eng., A **304-306**, 574 (2001).